


UNIMORE

UNIVERSITÀ DEGLI STUDI DI
MODENA E REGGIO EMILIA

"Enzo Ferrari" DEPARTMENT OF ENGINEERING

---

Master Degree in Electronics Engineering

# Near-Field Synthetic Aperture Radar Imaging Based on a MIMO FMCW Radar

Supervisor:
**Prof. Giorgio Matteo Vitetta**

Candidate:
**Alessandro Muratori Casali**

Co-Supervisors:
**Dr. Pasquale Di Viesti**

---

Academic Year 2025-2026

# Abstract

*Synthetic aperture radar* (SAR) imaging has traditionally relied on the assumption that the target lies in the far field of the radiating antenna, where the impinging wavefronts can be approximated as locally planar. However, in a growing number of short-range applications, including security screening, non-destructive testing, and compact biomedical imaging, targets are located within the near field of the antenna. In this case, the pronounced spherical curvature of the wavefronts invalidates the conventional far-field approximation and introduces a coupling between the range and cross-range dimensions of the imaging problem.

This Thesis reviews the fundamental principles of far-field SAR imaging and extends the theoretical framework to the near-field regime. A near-field signal model is derived, together with the corresponding resolution limits, and focusing strategies based on the angular spectrum method and time-domain back projection are investigated. The resulting near-field imaging framework is experimentally implemented using a 60 GHz *frequency-modulated continuous-wave* (FMCW) *multiple-input multiple-output* (MIMO) radar combined with a *mechanical scanning system*. Image reconstruction is performed using the *back projection algorithm* and further refined through a *minimum entropy autofocus* stage aimed at compensating for residual phase errors.

The proposed system is validated on several experimentally acquired scenes containing both metallic and non-metallic objects. Image quality and geometric accuracy are assessed under both *single-input single-output* (SISO) and MIMO configurations. The experimental results demonstrate that near-field back projection, combined with entropy-based autofocus, enables accurate and high-resolution radar imaging at short ranges.

# List of Acronyms

| | |
|---|---|
| ADC | Analog-to-Digital Converter |
| BPA | Back Projection Algorithm |
| DFT | Discrete Fourier Transform |
| FFT | Fast-Fourier Transform |
| FMCW | Frequency-Modulated Continuous-Wave |
| IF | Intermediate Frequency |
| MEA | Minimum Entropy Autofocus |
| MIMO | Multiple-Input Multiple-Output |
| RCS | Radar Cross-Section |
| RF | Radio Frequency |
| RX | Receiver |
| SAR | Synthetic Aperture Radar |
| SISO | Single-Input Single-Output |
| SNR | Signal-to-Noise Ratio |
| TDM | Time-Domain Multiplexing |
| TX | Transmitter |

# Index

**Abstract** . . . i
**List of Acronyms** . . . ii

**1 Introduction** **1**

**2 Principles and Models** **3**
2.1 Principles of Radar . . . 3
2.1.1 Overview and Operational Concept . . . 3
2.1.2 Radar Block Scheme . . . 3
2.1.3 FMCW signal model . . . 5
2.1.4 Time-of-Flight and Range Measurement . . . 6
2.1.5 Near-Field and Far-Field Imaging Regimes . . . 7
2.1.6 Radar Cross Section . . . 8
2.2 Synthetic Aperture Radar model . . . 9
2.3 Image reconstruction algorithms . . . 10
2.3.1 Classic Back Projection Algorithm . . . 10
2.3.2 Proposed Back Projection Algorithm . . . 12
2.4 Image focusing algorithms . . . 13
2.4.1 Minimum Entropy Autofocus . . . 13

**3 Physical implementation** **16**
3.1 Radar configuration . . . 16
3.1.1 Time-Division Multiplexing . . . 17
3.2 Scanning structure . . . 18

**4 Experimental Results** **21**
4.1 First scene . . . 22
4.2 Second scene . . . 23
4.3 Third scene . . . 25
4.4 Fourth scene . . . 27
4.5 Numerical results . . . 30

**5 Conclusions** **31**
5.1 Possible applications . . . 31
5.2 Future improvements . . . 32

**Bibliography** **33**
**Appendix** . . . 34

# Chapter 1

# Introduction

Radar systems are active sensors that detect and locate objects by transmitting *radio frequency* (RF) signals and analyzing the echoes reflected by the targets. Since they rely on their own transmitted energy and operate at frequencies that propagate through fog, rain, and clouds with limited attenuation, they are a robust alternative to optical sensors. *Synthetic aperture radar* (SAR) extends radar sensing to imaging: a physically small antenna is moved along a known trajectory and the echoes acquired at successive positions are combined coherently, emulating a much larger antenna array and overcoming the resolution limit imposed by the physical antenna size. SAR was originally developed for airborne and spaceborne remote sensing, but the recent availability of compact, low-cost, highly integrated millimeter-wave *frequency-modulated continuous-wave* (FMCW) radar devices has made it attractive also for short-range applications such as security screening, non-destructive testing, and compact biomedical imaging.

In these applications the targets lie within the near field of the device, which makes the classical far-field algorithms almost inapplicable. These algorithms assume planar wavefronts, so that the round-trip distance can be linearized and the image obtained through a direct Fourier relationship. This holds only when the observation distance is much larger than the Fraunhofer distance of the aperture. At much shorter ranges the wavefront curvature impact directly the received signal, and the exact distance between each antenna position and each image point must be taken into account. The *back projection algorithm* (BPA) serves this scope and is therefore well suited to the near field, but it is computationally expensive. On the contrary, Fourier-domain formulations [11] reduce the processing time considerably, at the cost of a lower accuracy in the range compression. A further difficulty is the phase accuracy of the data: at 60 GHz the scanning step must not exceed a quarter of the wavelength (1.25 mm) so that mechanical positioning errors, calibration mismatches between the antennas, and unwanted echoes introduce phase errors and defocus the image. Autofocus algorithms compensate such errors directly from the data, and *minimum entropy autofocus* (MEA) has the advantage of operating on the intensity distribution of the image, without requiring isolated dominant scatterers [9, 8, 12, 4].

The objective of this Thesis is to design, implement, and experimentally validate a system for near-field SAR image reconstruction based on a low-cost millimeter-wave MIMO radar and a simple mechanical scanning structure. The acquisition

system combines the IWR6843AOP 60 GHz radar, operated in *time-division multiplexing* (TDM), with a three-axis structure that scans the target on a grid whose step is derived from the sampling criterion. The images are reconstructed with the BPA and with a computationally efficient Fourier-domain variant for MIMO radars based on [11], and are then refined by a MEA stage that estimates a scalar phase correction for each acquired frame. The system is validated on four scenes containing metallic and non-metallic objects, placed at the same or at different distances from the radar, comparing a SISO-equivalent configuration with a MIMO one, and the images obtained with BPA alone with those obtained after MEA, both visually and through the image entropy.

The Thesis is organized as follows:

- **Chapter 2** presents the principles of FMCW radar, the near-field and far-field regimes, the SAR signal model, the reconstruction algorithms, and the MEA.
- **Chapter 3** describes the physical implementation, namely the radar configuration, the TDM scheme, the mechanical scanning structure, and the acquisition procedure.
- **Chapter 4** reports and compares the results obtained on the four test scenes, including a numerical comparison based on the image entropy.
- **Chapter 5** draws the conclusions and discusses possible future developments.
- Finally, the appendices detail the range compression through the *Discrete fourier transform* (DFT) and the derivation of the maximum admissible step of the scanning grid.

# Chapter 2

# Principles and Models

## 2.1 Principles of Radar

### 2.1.1 Overview and Operational Concept

The acronym **RADAR** stands for *RAdio Detection And Ranging*. A radar system is an active electromagnetic sensor used to detect, locate, track, and identify objects, called *targets*, at a certain distance. The system operates by emitting RF signals, through one or more antennas, into space and analyzing the *echo* signal reflected back from the target.

Radar systems offer key operational advantages over others [6]:

- **All-weather capability:** Radar operating frequency electromagnetic waves propagate through cloud cover, fog, rain, and atmospheric turbulence with relatively low signal loss.
- **Day/night operation:** Because the system relies on its own transmitted energy, performance is independent of natural illumination.
- **Direct kinematic estimation:** Can achieve high-precision range, angular direction, and radial velocity estimation directly from signal delay, spatial beam steering, and Doppler shifts with very well known methods.

This characteristics make a radar device very convenient in some application where others would fail consistently.

### 2.1.2 Radar Block Scheme

A general overview of the radar architecture is presented in Figure 2.1. The system is composed of a transmitter chain, a receiver chain, and a set of shared digital and control blocks that synchronize signal generation and data acquisition [2].

#### Transmitter

The transmitter chain is responsible for generating the FMCW chirp signal and radiating it toward the scene. Its main blocks are the following:

- **Waveform Generator (Synthesizer):** A frequency synthesizer, typically based on a *phase-locked loop*, generates a linear frequency ramp (*chirp*) starting at the frequency $f_0$ and sweeping over the bandwidth $B$ in a time $T$, according to Equation (2.3). The linearity of this ramp directly affects the achievable range resolution.

- **Power Amplifier (PA):** The generated chirp is amplified to the power level required for transmission, compensating for the losses introduced by the subsequent stages and by the antenna itself.

- **Transmitting Antenna (TX):** The amplified signal is radiated toward the scene by one or more transmitting antenna elements. In a MIMO configuration, such as the one described in Section 3.1, multiple transmitting elements are sequentially or orthogonally activated (e.g., via TDM) so that each transmitter–receiver pair contributes a distinct virtual antenna element.

A local copy of the transmitted chirp is also routed internally to the receiver chain, where it is used as a reference signal for the dechirping (mixing) operation described below.

### Receiver

The receiver chain collects the signal backscattered by the scene and converts it into a baseband signal suitable for digitization. Its main blocks are:

- **Receiving Antenna (RX):** Each receiving element captures the echo signal reflected by the target, delayed with respect to the transmitted chirp by the round-trip time $\tau$ defined in Equation (2.16).

- **Low-Noise Amplifier (LNA):** The received echo, typically very weak due to the propagation losses and the small *radar cross section* (RCS) of the target, is amplified while introducing minimal additional noise, in order to preserve the *signal-to-noise ratio* (SNR) of the acquisition.

- **Mixer (Dechirping):** The amplified received signal is downconverted to an *intermediate frequency* (IF) by mixing it with a copy of the transmitted chirp. Since both signals share the same linear frequency ramp, the result of this operation is a tone at a constant *beat frequency* ($f_{beat}$), proportional to the round-trip delay $\tau$ (and hence to the target range), as illustrated in Figure 2.2. This dechirping operation is what allows an FMCW radar to achieve high range resolution using relatively inexpensive, low-bandwidth analog-to-digital converters.

- **Low-pass filter:** A low-pass (or band-pass) filter removes out-of-band noise and unwanted mixing products, isolating the low frequency spectrum before digitization.

- **Analog-to-Digital Converter (ADC):** The filtered IF signal is sampled and quantized, producing the discrete-time data stream.

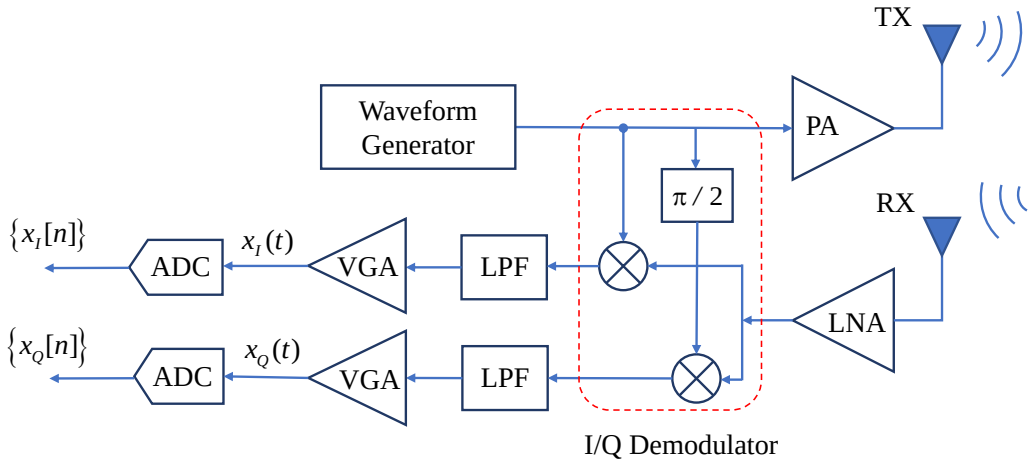



Figure 2.1: Typical block scheme for a radar device [5].

After these steps, the data are further processed to retrieve information about range, velocity or angle of arrival.

### 2.1.3 FMCW signal model

The system employs a FMCW chirp signal; this type of signal is characterized by a linear increase of the frequency during the transmission, as shown in Figure 2.2. During a single frame, multiple chirp signals can be transmitted, usually to average the samples or to make velocity estimation.

The generated signal is composed as $s(t) = s_I(t) + js_Q(t)$, where the in-phase component is expressed as

$$s_I(t) = \cos(2\pi(f_0 + \frac{1}{2}\mu t)t), \tag{2.1}$$

and the quadrature component, shifted by a phase of $-\pi/2$ with respect to the previous one, is expressed as

$$s_Q(t) = -\sin(2\pi(f_0 + \frac{1}{2}\mu t)t), \tag{2.2}$$

with $t \in [0, T)$, where $f_0$ is the signal frequency at time $t = 0$, $\mu$ is the slope of the frequency with respect to time and $T$ is the chirp duration. The slope is computed as $\mu = B/T$, where $B$ is the total sweep bandwidth, defined as $B = f_{max} - f_0$. The instantaneous frequency is therefore

$$f = f_0 + \mu t. \tag{2.3}$$

The transmitted signal can be expressed as a complex exponential in the following form

$$s_{TX}(t) = e^{j2\pi(f_0 + \frac{1}{2}\mu t)t}. \tag{2.4}$$

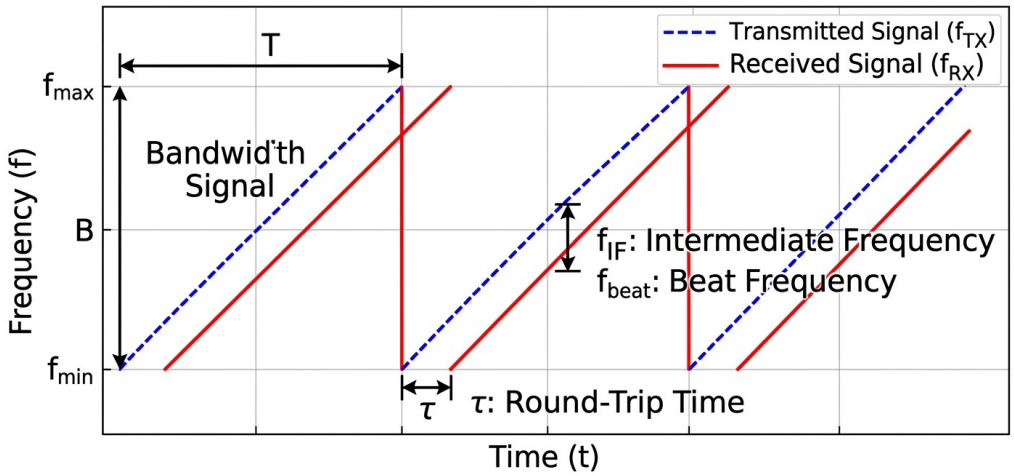



Figure 2.2: General FMCW signal with three ramps.

Once the generated signal is propagated, it will be back reflected by the target, so the received signal is a time-delayed copy of the transmitted one, and can be expressed as

$$s_{RX}(t) = \alpha \cdot \exp(j2\pi((f_0 + f_D)(t-\tau) + \frac{1}{2}\mu(t-\tau)^2)), \tag{2.5}$$

where $\tau$ is the round-trip delay and $\alpha$ is a real term that accounts for the amplitude reduction of the received wave. Since the received signal is downconverted with a mixer and filtered, the peak in the spectrum, corresponding to the target, will be at a frequency

$$f_{beat} = f_{tx} - f_{rx} = \mu \cdot \tau, \tag{2.6}$$

where $f_{tx}$ is the transmitted signal and $f_{rx}$ is the received one. Note that the computation is done without considering the effect of the Doppler shift $f_D$, assuming so that the target object is not moving.

Once the beating frequency is recovered from the received signal, it is possible to compute the target distance since $f_{beat}$ is proportional to the round-trip delay $\tau$, as

$$f_{beat} = \frac{2B \cdot R}{cT} \Rightarrow R = \frac{cT f_{beat}}{2B}, \tag{2.7}$$

in this way it is possible to recover distance information from the backscattered signal. Note that it is possible only because the frequency of the chirp is changing in time; it would not be possible to make range estimation using, for example, a *Continuous wave* radar because it only transmits a single frequency signal.

### 2.1.4 Time-of-Flight and Range Measurement

The radial distance (range, $R$) from the radar antenna to a target is determined by measuring the round-trip delay $\tau$ of the transmitted signal, traveling at the speed of light $c \approx 3 \times 10^8$ m/s.

Because the electromagnetic wave travels from the transmitter to the target and back to the receiver, the total distance traversed is $2R$. Thus, the fundamental range equation is

$$R = \frac{c \cdot \tau}{2}. \tag{2.8}$$

As shown in Section 2.1.3, in a FMCW radar the round-trip delay $\tau$ is not measured directly, but is instead recovered from the beat frequency ($f_{beat}$) produced by the dechirping operation, through Equation (2.7). This approach, however, is only valid under the assumption that the target echo is received within the same chirp period during which it was transmitted, that is $\tau \ll T$. If this condition is not met, the echo from a given chirp is mixed with the ramp of a subsequent one, and the resulting beat frequency no longer corresponds to the actual target range, producing a *range ambiguity*. This sets a first, practical limit on the maximum measurable range,

$$R_{\text{max,chirp}} \approx \frac{c \cdot T}{2}. \tag{2.9}$$

A second, generally more restrictive limit is imposed by the sampling rate $f_s$ of the ADC. Since the beat frequency $f_{beat}$ must be correctly represented in the digitized signal, the Nyquist criterion requires $f_{beat} \leq f_s/2$. Using Equation (2.6), this translates into an upper bound on the measurable round-trip delay, and consequently on the maximum unambiguous range

$$R_{\text{max}} = \frac{c \cdot T \cdot f_s}{4B}. \tag{2.10}$$

In practice, the smaller of the two values given by Equations (2.9)–(2.10) determines the actual *maximum unambiguous range* of the system. If a target is located beyond this limit, its echo is either not correctly captured within the chirp duration or aliased into a lower apparent beat frequency, causing it to appear as a closer target and introducing range ambiguities in the reconstructed data.

The theoretical *range resolution* ($\Delta R$), which defines the minimum separation in range required to distinguish two targets individually, depends only on the total swept bandwidth $B$ of the chirp, and is given by

$$\Delta R = \frac{c}{2B}. \tag{2.11}$$

This result follows directly from the width of the main lobe of the range-compressed signal, and it is independent of the chirp duration $T$ or the carrier frequency $f_0$: increasing the bandwidth $B$ narrows the beat-frequency resolution cell and therefore improves the ability to separate closely spaced targets in range.

### 2.1.5 Near-Field and Far-Field Imaging Regimes

Before addressing the image reconstruction algorithms in Section 2.3, it is useful to characterize the propagation regime in which the acquisition described in this work takes place, since this determines which class of reconstruction algorithms can be correctly applied.

When a synthetic aperture of maximum dimension $D$ observes a target at range $R$, the wavefronts impinging on the aperture can be approximated as locally planar only if $R$ is sufficiently large compared to $D$ and to the wavelength $\lambda$. This condition defines the classical distinction between the *near field* and the *far field* of the aperture. The boundary between the two regimes is conventionally set by the Fraunhofer distance [1]

$$R_F = \frac{2D^2}{\lambda}. \tag{2.12}$$

For $R \gg R_F$, the aperture operates in the *far field*: the phase of the wavefront across the aperture is well approximated by a linear function of position, and the round-trip distances $R_T$ and $R_R$ introduced in Equation (2.15) can be linearized with respect to the scanning coordinates. Under this approximation, the phase history collected by the synthetic aperture becomes a simple linear function of the scanning position and of the target angle, and the reflectivity function can be recovered efficiently through a direct two-dimensional Fourier transform relating the wavenumber domain $(k_x, k_y)$ to the spatial domain $(x, y)$, without needing to evaluate the exact distance to every point of the scene.

For $R \lesssim R_F$, the aperture instead operates in the *near field*: the curvature of the wavefront across the aperture is no longer negligible, and the linear approximation of $R_T$ and $R_R$ is no longer valid [10]. In this regime, the exact expressions of Equation (2.15) must be retained for every combination of antenna position and target point, since the quadratic (and higher-order) phase terms neglected in the far-field approximation become significant with respect to the operating wavelength and introduce noticeable defocusing if ignored.

### 2.1.6 Radar Cross Section

The RCS, denoted by $\sigma$, is a measure of a target's ability to reflect radar signals back in the direction of the radar receiver. Formally, it represents the fictitious area that would intercept an amount of incident power such that, if that intercepted power were scattered isotropically in all directions, it would produce an equivalent power density at the receiver as the actual target.

It is important to emphasize that RCS does not strictly correspond to a target's physical surface area. An aircraft with a large physical cross-section can be engineered using stealth techniques to present a very small RCS, whereas a small metal sphere can exhibit a disproportionately large RCS due to its strong reflections.

In the far-field limit, the RCS of a target is defined mathematically as [3]

$$\sigma = \lim_{R\to\infty} 4\pi R^2 \frac{|E_s|^2}{|E_i|^2} = \lim_{R\to\infty} 4\pi R^2 \frac{S_s}{S_i} \tag{2.13}$$

where:

- $R$ is the distance between the radar and the target,
- $E_i$ and $E_s$ are the complex electric field amplitudes of the incident and scattered waves, respectively,

- $S_i$ and $S_s$ are the incident and scattered power flux densities at the target and receiver.

The factor $4\pi R^2$ corresponds to the surface area of a sphere of radius $R$, accounting for isotropic spherical spreading of the scattered wave as it propagates back to the radar.

RCS is a fundamental parameter in determining target detectability. In the classic monostatic radar range equation, the received power $P_r$ is directly proportional to $\sigma$:

$$P_r = \frac{P_t G_t G_r \lambda^2 \sigma}{(4\pi)^3 R^4} \tag{2.14}$$

where $P_t$ is the transmitted power, $G_t$ and $G_r$ are the transmitter and receiver antenna gains, $\lambda$ is the radar operational wavelength, and $R$ is the distance to the target.

Key factors influencing a target's RCS include geometric shape and aspect angle, material composition (such as radar-absorbing materials or metallic conductors), signal polarization (e.g., *horizontal-horizontal*, HH, *vertical-vertical*, VV), and radar operating frequency.

## 2.2 Synthetic Aperture Radar model

The SAR working concept is to employ a radar device, with reduced dimensions, to simulate a much larger antenna array; this is possible by measuring the backscattered data in multiple positions along the scanning axis.

In this section the wave propagation model of the backscattered SAR data is presented, following from the signal model discussed in Section 2.1.3.

In case of a single scatterer at position ($x$, $y$, $z$), considering the transmitter position at ($x_T$, $y_T$, $Z_0$) and the receiver one at ($x_R$, $y_R$, $Z_0$), it is possible to define [11]

$$\begin{aligned} R_T &= \sqrt{(x - x_T)^2 + (y - y_T)^2 + (z - Z_0)^2}, \\ R_R &= \sqrt{(x - x_R)^2 + (y - y_R)^2 + (z - Z_0)^2}, \end{aligned} \tag{2.15}$$

that are respectively the target distance from the transmitting element and from the receiving one. So the round trip delay of the emitted wave $\tau$ is calculated as

$$\tau = \frac{R_T + R_R}{c}, \tag{2.16}$$

where $c$ is the speed of light.

The backscattered data collected by the receiving element can be then expressed, rearranging Equation (2.5), as

$$s(t - \tau) = \frac{\rho}{R_T R_R}(s_I(t - \tau) + j s_Q(t - \tau)), \tag{2.17}$$

where $\rho$ is the complex reflectivity of the scatterer, and the amplitude decay term is modeled as $\alpha = \rho / R_T R_R$. Since the round trip delay is very small, the exponential

term $\exp(j\pi\mu\tau^2)$ called *residual video phase* is negligible, and therefore Equation (2.17) can be rewritten as

$$s(t-\tau) = \frac{\rho}{R_T R_R} e^{-j2\pi(f_0\tau+\mu\tau t)} = \frac{\rho}{R_T R_R} e^{-jkR_T} e^{-jkR_R}, \tag{2.18}$$

where $k = 2\pi f/c$ is the wavenumber corresponding to the instantaneous frequency.

## 2.3 Image reconstruction algorithms

The raw data acquired by a SAR system is a multi-dimensional array, sampled along the scanning dimensions with each ADC sample. This data must be elaborated to reconstruct the scanned scene. This procedure is done by coherently summing the complex image generated by every acquired sample, so that some pixels sum constructively and others in a destructive manner.

Multiple algorithms have been proposed in the literature, like the *Range Migration Algorithm*, *Range-Doppler*, the *Polar Format Algorithm* or the BPA.

In this work only the last one, described in Subsection 2.3.2, has been used due to its simplicity and precision.

### 2.3.1 Classic Back Projection Algorithm

The BPA is a well known and widely used algorithm for precise image reconstruction. The traditional algorithm is quite computationally expensive because it computes the distance between every pixel and every position of the antennas. The complete time domain algorithm, for a MIMO device to reconstruct the 3D image is explained in Algorithm 1.

The objective is to recover the reflectivity function $\rho(x, y, z)$ from the received backscattered data $s(x_T, x_R, y_T, y_R, k)$ as [11]

$$\rho(x,y,z) = \iiiint s(x_T, x_R, y_T, y_R, k) e^{jkR_T} e^{jkR_R}\, dx_T\, dx_R\, dy_T\, dy_R\, dk. \tag{2.19}$$

**Algorithm 1** Back projection algorithm steps

1: Define the 3D volume grid $g$ that will be reconstructed, whose dimensions are $[N_X, N_Y, N_Z]$.
2: **for** $i = 0 \rightarrow N_{STEPS}$ **do**
3: From the array $s$ containing the raw data take the samples corresponding to the $i$-th acquisition frame.
4: **for** $c_x = 0 \rightarrow N_X$ **do**
5: **for** $c_y = 0 \rightarrow N_Y$ **do**
6: **for** $c_z = 0 \rightarrow N_Z$ **do**
7: **for** $t_x = 0 \rightarrow N_{tx}$ **do**
8: **for** $r_x = 0 \rightarrow N_{rx}$ **do**
9: Compute the round-trip delay $\tau$ between the antennas and the considered grid point using Equations (2.15)–(2.16).
10: Calculate the range-compressed data using the DFT over the fast-time samples, at the range bin corresponding to $\tau$ (see Appendix 5.2).
11: Apply the phase correction $\phi_0 = e^{jk(R_T+R_R)}$, as in Equation (2.19), and accumulate the results.
12: **end for**
13: **end for**
14: **end for**
15: **end for**
16: **end for**
17: **end for**
18: **return** $\rho$

In the last part:

- $N_{STEPS}$ is the total number of acquired frames.
- $N_X$ is the number of X positions in the grid $g$.
- $N_Y$ is the number of Y positions in the grid $g$.
- $N_Z$ is the number of Z positions in the grid $g$.
- $N_{tx}$ is the number of transmitting elements used during the acquisition.
- $N_{rx}$ is the number of receiving elements used during the acquisition.

### Advantages and limitations

The short distance between the radar and the scanned target directly motivates the choice of reconstruction algorithm adopted in this work. Far-field imaging algorithms based on a direct Fourier relationship between the wavenumber domain and the image domain, such as the classical *Range-Doppler* or *Polar Format* algorithms, rely on the linear phase approximation discussed above and are therefore not directly applicable to the present configuration. The BPA method, instead computes the exact round-trip distance between every antenna position and every point of the

reconstructed grid, and is for this reason well suited to near-field imaging scenarios such as the one considered in this work, at the cost of the additional computational complexity.

### 2.3.2 Proposed Back Projection Algorithm

In this section, the BPA algorithm for a MIMO radar configuration is presented, based on a well known previous work [11]. This algorithm has the same underlying structure of the previous one but it differs a bit, as it was elaborated to enhance the computational burden and the time required to generate the image, at the cost of some accuracy.

By defining the matched filter, for every wavelength and target point, as

$$h(x, y, z, x_R, x_T, y_R, y_T, k) = e^{jkR_T} e^{jkR_R}, \tag{2.20}$$

it is possible to calculate the reflectivity function $p$ with the following equation

$$\rho(x, y, z) = \iiiii s(x_T, x_R, y_T, y_R, k) \times h(x, y, z, x_R, x_T, y_R, y_T, k)\, dx_T\, dx_R\, dy_T\, dy_R\, dk. \tag{2.21}$$

To improve the computational efficiency of the algorithm, it is possible to exploit the convolution property of the Fourier transform, that is, for two general functions $f$ and $g$

$$\mathcal{F}\{f(t) \times g(t)\} = F(\omega)G(\omega), \tag{2.22}$$

where $F$ and $G$ represent, respectively, the Fourier transform of the $f$ and $g$ functions, and the symbol $\times$ represent the convolution operation. So, by applying the Fourier transform to both the backscattered signal $s(x_T, x_R, y_T, y_R, k)$ and the matched filter $h(x, y, z, x_R, x_T, y_R, y_T, k)$, it is possible to rewrite equation (2.21) as

$$P(k_x, k_y, z) = \int S(k_x, k_y, k) H(k_x, k_y, z, k)\, dk, \tag{2.23}$$

where $P$, $S$ and $H$ are, respectively, the Fourier transforms with respect to both the $x$ and $y$ axis of $\rho$, $s$ and $h$; $k_x$ and $k_y$ are the corresponding wavenumber coordinates.

The final reconstructed reflectivity is then

$$\rho(x, y, z) = IFT_{2D}^{(k_x, k_y)}[P(k_x, k_y, z)], \tag{2.24}$$

where $IFT_{2D}^{(k_x, k_y)}$ is the 2-D inverse Fourier transform operation over the $k_x$- and $k_y$-domain.

#### Advantages and limitations

The presented method improves the total time required by a very large factor (over 1000x) with respect to the previous one. The trade-off is in the range compression over the fast-time samples of the acquired data, as in this case the Fourier transform is not computed for the precise range bin, but over a discrete set of bins using the well known *fast fourier transform* (FFT) (see Appendix 5.2). Although this is the only real compromise, it cannot be removed since it would require to compute the precise distance between the antennas and the target. This approach still allows to generate very clear images, as shown in Chapter 4.

## 2.4 Image focusing algorithms

The algorithms discussed in Section 2.3 serve the purpose of reconstructing the image based on the raw data, without considering some non-idealities. Such problems might be related to background noise, motion errors, calibration mismatches, echoes or some other minor causes, that induce phase errors in the acquired data. Objective of the so called *focusing algorithms*, is to further elaborate, from a raw data or image perspective, the results of the imaging algorithms, to achieve a higher accurate image.

In the literature some algorithms, like the well known *Phase Gradient Autofocus* (PGA), *Prominent Point Processing* or *Map drift*, have been proposed for classical SAR setups, but the majority of these cannot be implemented in the presented configuration due to different operating scenario. In this section only one algorithm is presented.

### 2.4.1 Minimum Entropy Autofocus

MEA is one of the most widely used approaches of this kind, originally proposed for *inverse SAR* imaging by Xi, Liu, and Ni [9] and subsequently adapted and refined for SAR by several authors [8, 12, 4]. In this section an inspired version of the known algorithm is presented, as it does not follows the same steps, but the underlaying concept remains the same.

#### Image Entropy as a Focus Metric

The underlying idea of MEA is that a well-focused image concentrates the reflected energy into a small number of bright, sharply defined pixels, whereas a defocused image spreads that same energy over a larger area, producing a smoother, more uniform intensity distribution. Shannon entropy provides a convenient scalar measure of this concentration: given a complex 3D SAR image $\rho(x, y, z)$, where $(x, y, z)$ denotes image grid coordinates, its total energy

$$E = \sum_x \sum_y \sum_z |\rho(x, y, z)|^2 \tag{2.25}$$

is invariant to any phase-only correction applied to the underlying signal history, by Parseval's theorem. Normalizing the pixel intensities by this total energy yields a probability-like distribution

$$p(x, y, z) = \frac{|\rho(x, y, z)|^2}{E} \tag{2.26}$$

whose entropy is defined as

$$H = -\sum_x \sum_y \sum_z p(x, y, z)\ \log_2 p(x, y, z) \tag{2.27}$$

A sharply focused image, with energy concentrated in few pixels, yields a low value of $H$, while a defocused image, with energy spread over many pixels, yields a higher value. MEA exploits this relationship by searching for the phase correction that minimizes $H$.

### Iterative Algorithm

As the original proposed algorithm it is iterative, but it follows a different procedure, explained in Algorithm 2.

The objective of the algorithm is to estimate, for each frame $i$, a scalar phase correction $\hat{\phi}_i \in \mathbb{R}$ such that the entropy $H$ of the corrected image, defined in Equation (2.27), is minimized. The problem is solved through an iterative scheme, in which the phase correction of a single frame is optimized at a time while keeping all the others fixed, and the procedure is repeated for a fixed number of iterations $N_{iter}$.

**Algorithm 2** Minimum entropy autofocus steps

1: Generate a first, possibly defocused, image $\rho(x, y, z) = \sum_i \rho_i(x, y, z)$ using any of the reconstruction algorithms of Section 2.3, retaining the per-frame contributions $\rho_i(x, y, z)$.
2: Define the discrete set of candidate phase corrections $\Phi = \{\phi_1, \ldots, \phi_M\}$.
3: **for** $j = 0 \to N_{iter}$ **do**
4:  **for** $i = 0 \to N_{STEPS}$ **do**
5:  Remove the current contribution of frame $i$ from the image, $\rho(x, y, z) \leftarrow \rho(x, y, z) - \rho_i(x, y, z)$.
6:  **for** $m = 1 \to M$ **do**
7:  Compute the phase-corrected contribution $\rho_i^{(m)}(x, y, z)$.
8:  Form the trial image $\rho^{(m)}(x, y, z)$ and compute its entropy $H^{(m)}$ using Equations (2.25)–(2.27).
9:  **end for**
10:  Select the optimal correction $m^* = \arg\min_m H^{(m)}$.
11:  Update the image and the stored contribution of frame $i$ as $\rho(x, y, z) \leftarrow \rho(x, y, z) + \rho_i^{m^*}(x, y, z)$
12:  **end for**
13: **end for**
14: **return** $\rho$

In the previous description:

- $N_{iter}$ is the number of times the correction sweep is repeated over the full set of frames.
- $N_{STEPS}$ is the total number of acquired frames.
- $M$ is the number of candidate phase corrections evaluated at each step.

### Advantages and Limitations

Compared to other well-known autofocus techniques, such as the PGA algorithm, which relies on the presence of isolated, dominant point scatterer to estimate the phase error, MEA operates directly on the image intensity distribution and therefore remains applicable to distributed or extended scenes lacking strong discrete reflectors. This generality, however, comes at the cost of a higher per-iteration computational burden, since the entropy must be calculated for every possible phase

corrected image at every iteration; this number scales linearly with the number $M$ of possible corrections and with the number of acquired frames $N_{STEPS}$. It is possible to iterate the algorithm an arbitrary number of times $N_{iter}$, considering that the total processing time will obviously increase by a factor corresponding to this number, and if it too large it can create distortions in the image, as this algorithm operates directly on the data without knowing anything about the reconstructed scene. These limitations have motivated a number of extensions in the more recent literature, including adaptive step-size strategies, sparsity-assisted formulations that improve robustness at low signal-to-noise ratios, and applications to moving-target refocusing, which build on the same underlying entropy-minimization principle described above.

# Chapter 3

# Physical implementation

In this chapter, the setup that has been used for the realization of the measurement will be presented in detail. In particular, the radar device and the mechanical scanning structure will be described.

## 3.1 Radar configuration

For this work, the IWR6843AOP radar [7] has been used. It is a MIMO radar that works at a frequency $f_0 = 60$ GHz. It has three transmitting elements and four receiving ones, disposed as in Figure 3.1, so the total maximum number of virtual elements is $N_{ve} = N_t \cdot N_r = 12$, since there are no overlapping elements. Throughout the experiments only two transmitting elements, in particular *TX1* and *TX3*, have been used, so the real total number of virtual elements is $N_{ve} = 2 \cdot 4 = 8$.

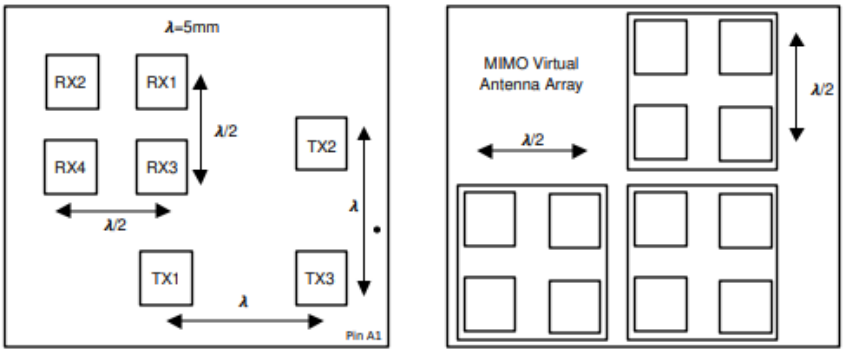



Figure 3.1: Antenna positions on IWR6843AOP radar [7].

The device parameters that have been used are reported in Table 3.1.

The effective bandwidth $B$ is smaller than the theoretical bandwidth swept by the ramp because the ADC does not sample the entire ramp time $t_{ramp}$, but only a fraction of it. As discussed in Section 2.1.3, the frequency synthesizer requires a settling interval, indicated by the ADC start time ($t_{ADC}$), before the generated chirp reaches a sufficiently linear behavior to be usable for sampling; the ADC is therefore enabled only after this initial delay has elapsed. Furthermore, the ADC captures a fixed number of samples $N_{samples}$ at a sampling frequency $f_s$, so that the actual sampling window has a duration of $(N_{samples} - 1)/f_s \approx 30$ $\mu$s, which is shorter than

the total ramp time $t_{ramp} = 38.7$ $\mu$s. Since the chirp slope $\mu$ is constant throughout the ramp, the effective bandwidth actually captured by the ADC can be computed as

$$B = \mu \cdot \frac{N_{samples} - 1}{f_s} \approx 80 \text{ MHz}/\mu\text{s} \cdot 30 \ \mu\text{s} \approx 2.4 \text{ GHz}, \tag{3.1}$$

which is consistent with the value reported in Table 3.1, and noticeably smaller than the theoretical bandwidth $\mu \cdot t_{ramp} = 3.096$ GHz swept over the full ramp duration. The portion of the ramp not exploited by the ADC, corresponding to the initial settling delay $t_{ADC}$, is therefore discarded, which slightly degrades the theoretical range resolution $\Delta R = c/(2B)$ achievable with respect to the nominal system bandwidth.

| Parameter | Value |
|---|---|
| Transmitting elements | 2 |
| Receiving elements | 4 |
| Start frequency $f_0$ | 60 GHz |
| Theoretical bandwidth | 3.096 GHz |
| Effective bandwidth $B$ | 2.4 GHz |
| ADC sampling frequency $f_s$ | 2.1 MS/s |
| Chirp slope $\mu$ | 80 MHz/$\mu$s |
| ADC samples per chirp $N_{samples}$ | 64 |
| Doppler chirp number | 8 |
| Rising time $t_{rise}$ | 30$\mu$s |
| Ramp time $t_{ramp}$ | 38.7$\mu$s |
| ADC start time $t_{ADC}$ | 7$\mu$s |
| Idle time $t_{idle}$ | 10$\mu$s |
| Range resolution $\Delta R$ | 6.25 cm |

Table 3.1: Radar configuration parameters.

### 3.1.1 Time-Division Multiplexing

MIMO radar systems employ $N_{tx}$ TX antennas and $N_{rx}$ RX antennas to synthesize a virtual antenna array.

To synthesize this virtual array, the signals originating from different TX antennas must be orthogonal at the receiver. Signal separation allows the receiver to isolate the individual propagation paths from each TX-RX antenna pair.

The TDM is a technique to make the different signals mutually orthogonal by activating transmit antennas sequentially in non-overlapping time slots. It is widely used in a variety of applications due to its simplicity and effectiveness.

In a FMCW system, TX antennas transmit identical linear frequency chirps in a time-multiplexed sequence. For a frame containing $M$ chirps and $N_{tx}$ transmit antennas, the $m$-th TX antenna ($m \in \{0, 1, \ldots, N_{tx}-1\}$) transmits at time intervals:

$$t \in [k \cdot N_{tx} \cdot T + mT, \ k \cdot N_{tx} \cdot T + (m+1)T] \tag{3.2}$$

where $T$ is the chirp duration and $k$ is the frame repetition index.

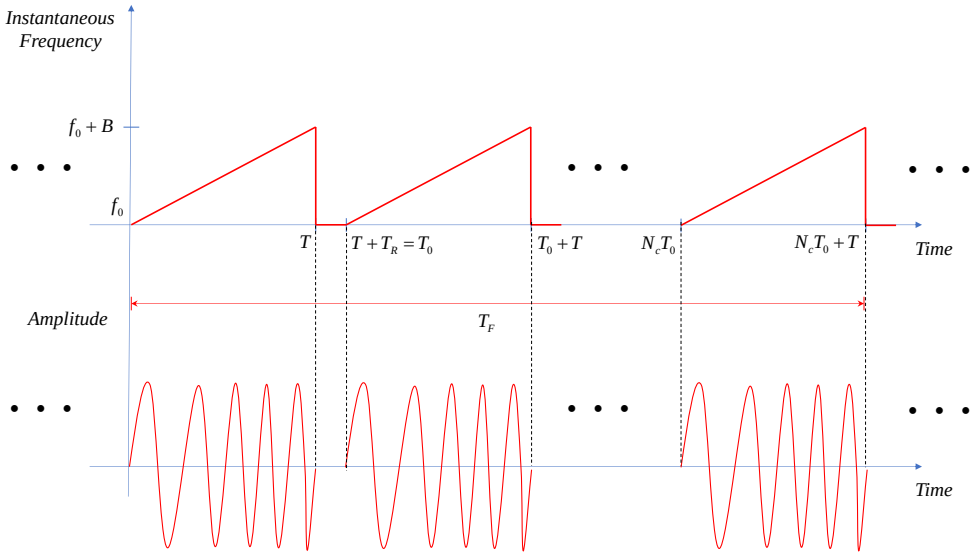



Figure 3.2: TDM-MIMO transmission sequence showing sequential chirp emission across $N_{tx}$ transmit channels [5].

The received signal at the $n$-th RX antenna ($n \in \{0, 1, \ldots, N_{rx} - 1\}$) corresponding to the $m$-th TX channel is processed by matched filtering or range-FFT during the active interval of $\text{TX}_m$.

Because only one TX antenna is active at any given moment, cross-talk and mutual interference between transmitters are minimized, simplifying hardware design. The only drawbacks are the time required, negligible in the case of this work, and the lower average SNR with respect to more complex techiques.

## 3.2 Scanning structure

To scan mechanically the scene, the structure in Figure 3.3 has been used. The main components are:

- **Stepper motors**: three stepper motors, one for each axis, that move mechanically the structure. The X-axis and the Y-axis motors move the bottom plate on which the objects that need to be scanned are placed.
- **Arduino board**: it controls the motor drivers. It is controlled via serial communication using a series of commands known as *geometric-code*. G-code is the standard *numerical control* programming language used to instruct automated machine tool, including CNC mills, lathes, 3D printers, laser cutters, and routers, how to move, at what speed, and along which paths.
- **Radar support**: it keeps the radar still while the bottom plate is moving. The Z-axis motor could be used to move the radar support up or down.

Moving the radar on the Z-axis would have improved further the results, but during this work it was not used, mostly because it would have increased the total scanning time by a factor equal to the number of Z-axis steps.

To reduce undesired echoes and improve the performance of the setup, an RF absorbing panel, with dimensions $21 \times 21$ cm, has been placed on the moving platform, on top of which the scanned object are lean on.

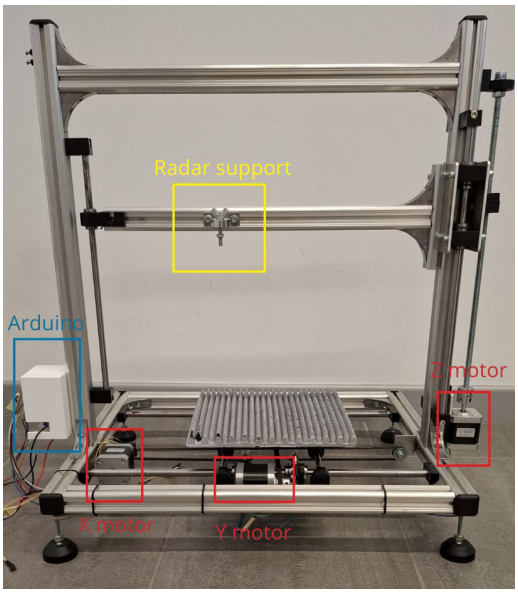



Figure 3.3: Front photo of the mechanical structure.

As shown in Figure 3.3, the maximum scanning dimensions are 22 cm for the X-axis and 19 cm for the Y-axis.

Since the step dimension in both X and Y direction is related to the wavelength value as $d_x = d_y = \frac{\lambda}{4}$ (see Appendix 5.2 for further details), using a 60 GHz radar device means that the length of each step should be $d_x = d_y = c/4f_0 = 1.25$ mm. This means that the stepper motors needed to be precisely calibrated, as the minimum motion error would lead to imprecise image reconstruction. During the first phase of this work, the steps of each motors have been calibrated with a sub-mm precision ($\sim 1/20$ mm), to reduce as much as possible motion errors.

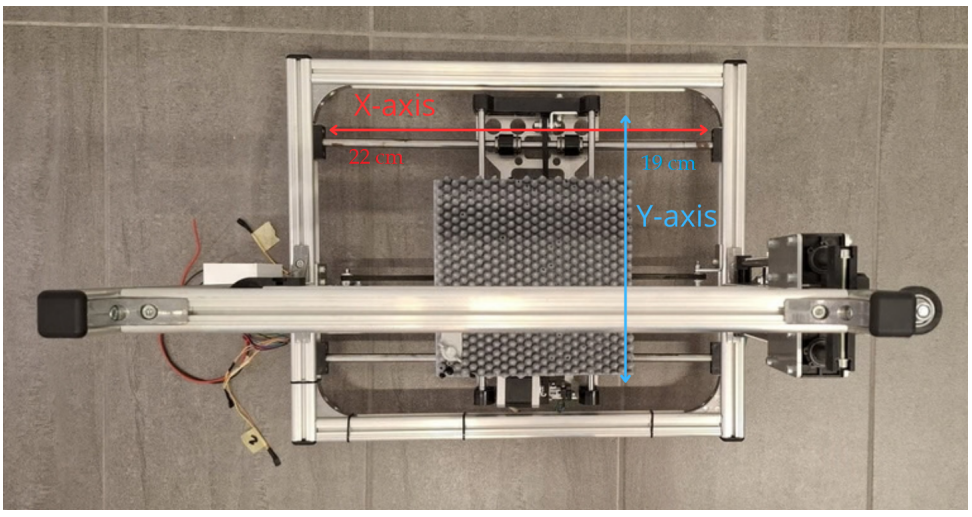



Figure 3.4: Upper photo of the mechanical structure.

The acquisition procedure is described in Algorithm 3. It accounts for the mechanical displacement along the three scanning axes and for the use of a MIMO radar device configured to transmit a single chirp per frame.

**Algorithm 3** Acquisition procedure

Initialize the raw-data array $s$ of dimensions $[X_{STEPS}, Y_{STEPS}, Z_{STEPS}, N_{tx}, N_{rx}, N_{sample}]$.
**for** $i = 0 \rightarrow X_{STEPS}$ **do**
  **for** $j = 0 \rightarrow Y_{STEPS}$ **do**
    **for** $k = 0 \rightarrow Z_{STEPS}$ **do**
      Move the radar to the position corresponding to the grid indices $(i, j, k)$.
      **for** $t_x = 0 \rightarrow N_{tx}$ **do**
        **for** $r_x = 0 \rightarrow N_{rx}$ **do**
          Acquire the raw data corresponding to the transmitting element $t_x$ and the receiving element $r_x$.
          Store the acquired samples in $s[i, j, k, t_x, r_x, :]$.
        **end for**
      **end for**
    **end for**
  **end for**
**end for**
**return** $s$

The quantities appearing in Algorithm 3 are defined as follows:

- $X_{STEPS}$, $Y_{STEPS}$, and $Z_{STEPS}$ denote the total number of discrete positions along the $X$-, $Y$-, and $Z$-axis, respectively, at which the radar data are acquired.
- $N_{tx}$ and $N_{rx}$ denote, respectively, the number of transmitting and receiving elements employed during the acquisition.
- $N_{sample}$ denotes the number of ADC samples acquired for each chirp signal.

# Chapter 4

# Experimental Results

The setup presented in Chapter 3 was tested on four different scenes, each characterized by different shape, material, or position of the targets. Such a variety has been exploited in order to assess the accuracy of the system under various real-world conditions. Inside the working environment, that was an office in which some people were actively working, the mechanical structure was placed on a table. This might have induced some echoes or unwanted mechanical movements. Moreover the presence of others scatterers, like the metallic scanning structure itself that was very close to the scanned scene, could have generated unwanted echoes. Both of these factors may have influenced the collected data.

The results will show the reconstructed images considering two operational cases: the "*SISO*" one implies the use of antennas *TX1* and *RX1* exclusively; the "*MIMO*" one implies almost full usage on the antennas, since antenna *RX4* was excluded due to some introduced distortions. The reported results labeled as *MIMO* will therefore be generated using the data from all the transmitting antennas and only the first three receiving ones.

In the following sections, visual images of the considered scenes will be first shown, then the reconstructed images using only the BPA algorithm described in Section 2.3.2, and finally the focused images generated using the MEA algorithm described in Section 2.4.1 in order to have a full comparison of the results. In the last section a numerical comparison of the results is given.

During the scanning procedure, described in Section 3.2, only one level for the Z-axis was configured, so the variable $Z_{STEPS} = 1$. Moreover during all the acquisitions, except for the second one(see Section 4.2), the RF absorbing panel has been used.

During the MEA processing only one iteration over each frame was computed, mostly due to the time necessary to elaborate the image, but also because for higher values of $N_{iter}$ there were some distortions.

Note that the color brightness in the reconstructed images is in a relative scale, not in an absolute one; this implies that, visually and mathematically, the lower entropy can be noticed when the contrast between the brightest pixels and the least ones is higher, as after the minimum entropy processing.

In the following sections 4.1-4.4 the results are compared in a visual way, while in Section 4.5 the results of a numerical comparison are discussed.

## 4.1 First scene

The first acquisition has been performed with two metallic objects of different shapes placed at the same distance level from the radar, as shown in Figure 4.1.

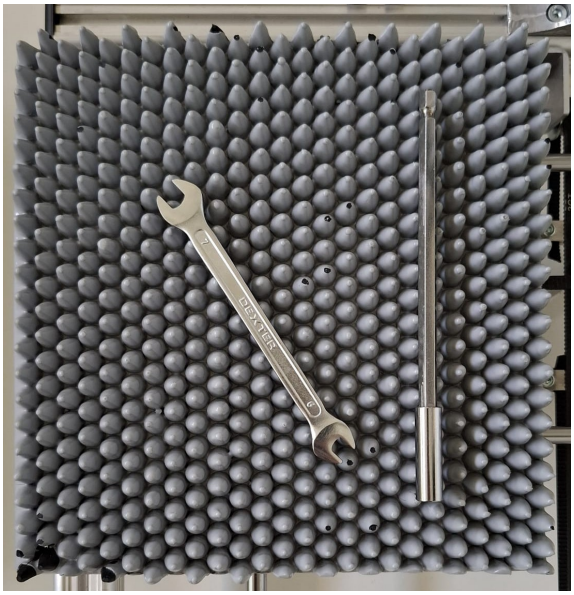
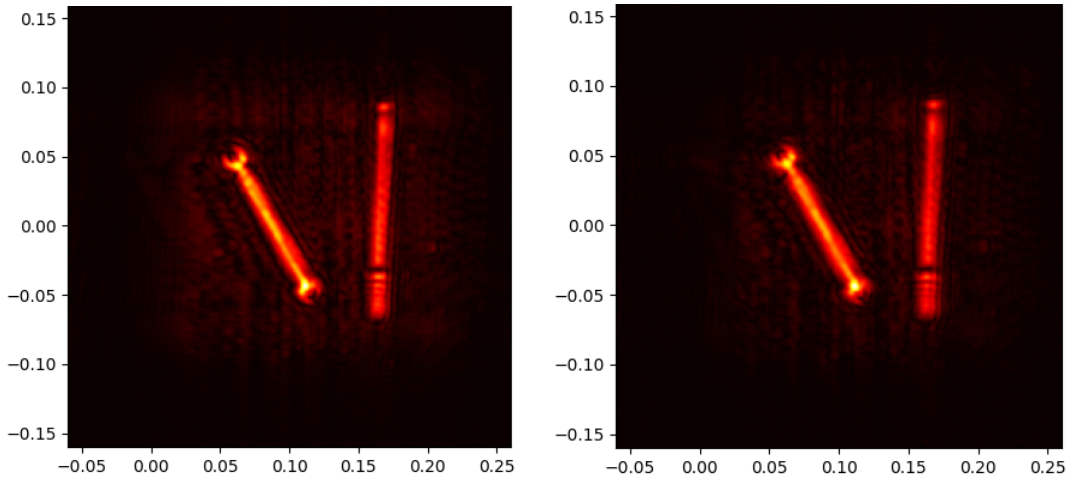


Figure 4.1: First test acquisition with two metallic objects.

This type of scanning scene is expected to generate a good quality image, since the two objects are metallic and therefore generate strong echoes. In addition, they are on the same level and quite distanced; this should limit the amount of noise in the image.

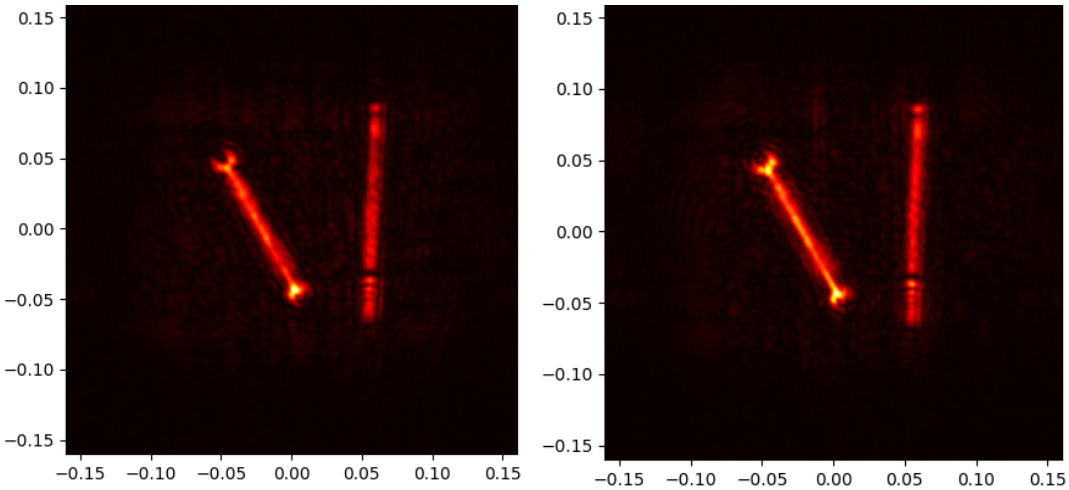



(a) MIMO BPA result (b) SISO BPA result

Figure 4.2: Imaging results of the first scene using only BPA.

As expected, the scene is clearly visible in the reconstructed image in both cases. In the MIMO result, shown in Figure 4.2a, the image is slightly more noisy, generating, however, a distinguishable image of the two objects.

The result of the SISO imaging (Figure 4.2b) is, instead, clearly visible and already quite focused, as there is almost no energy dispersed in the image other than the two objects.




(a) MIMO MEA result (b) SISO MEA result

Figure 4.3: Imaging results of the first scene using MEA.

After applying the MEA algorithm, the results, shown in Figure 4.3a and Figure 4.3b, are high contrast images where almost all the energy is concentrated on the objects. As expected, the residual shadows of the BPA images is almost totally removed, leaving a very clear vision of the scene.

## 4.2 Second scene

For the second acquisition, an object with a more detailed and complex shape was chosen, as shown in Figure 4.4, to test the system's ability to recognize finest features. Also in this case the object was metallic.

Note that in this case the scan was incomplete due to some time constraint, so it is reasonable to presume that even a higher quality of the results could be achieved with a full scan. Moreover, the RF absorbing panel was not used because the chosen object was the actual moving platform of the scanning structure.

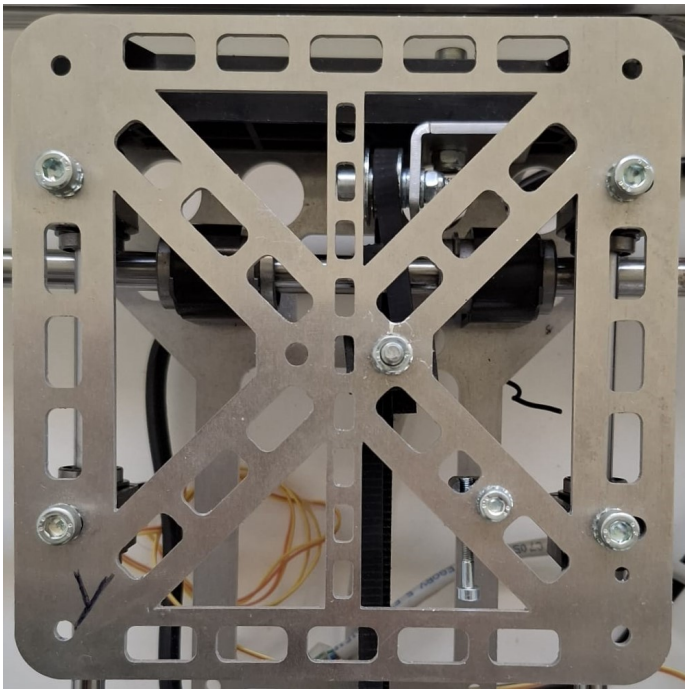
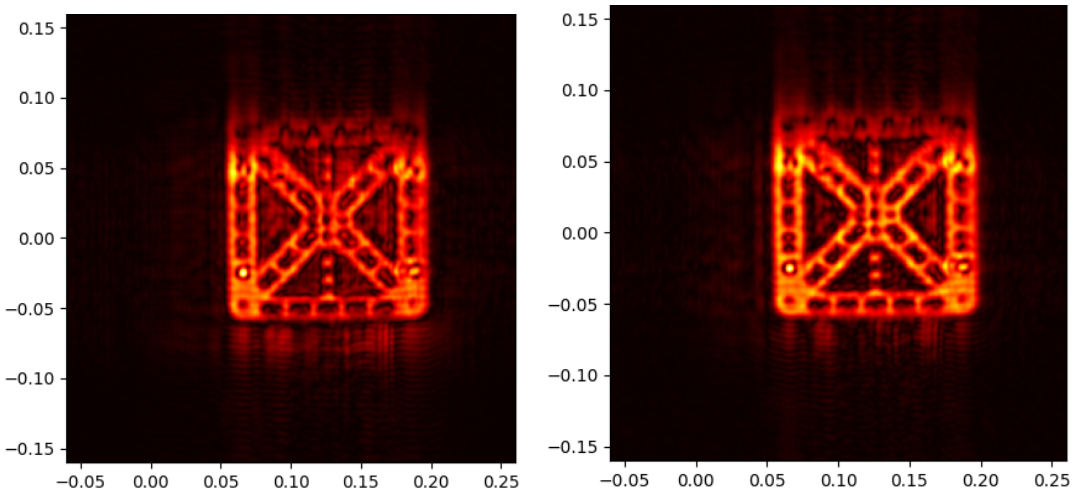


Figure 4.4: Second test acquisition with a complex metallic object.

As in the previous case (Section 4.1), the results are expected to show a good representation of the object, despite some small features, due to its metallic nature.

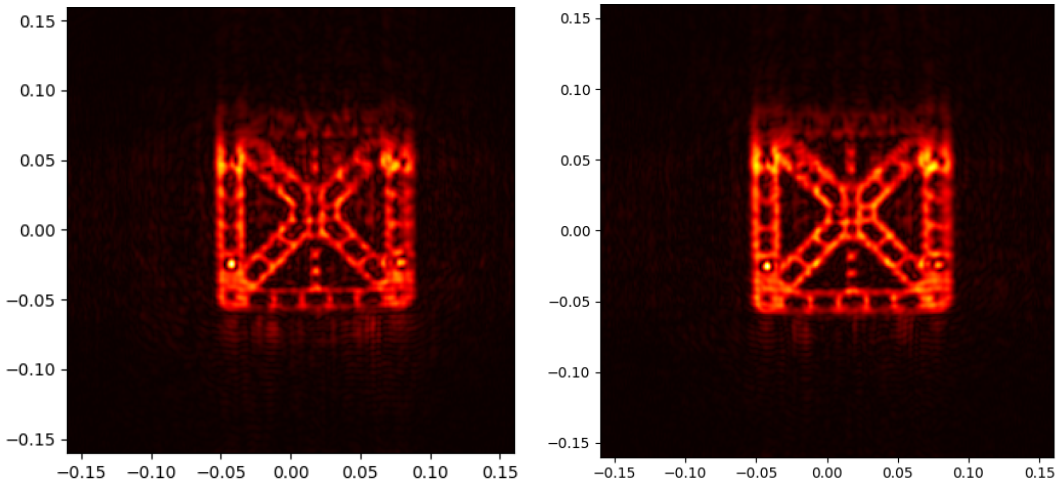



(a) MIMO BPA result

(b) SISO BPA result

Figure 4.5: Imaging results of the second scene using only BPA.

As in the previous results, the image considering the MIMO case is noisier than the SISO one. Although the shape of the object is easily recognizable in both cases, the smallest details in the middle segment are not fully clear. However, even these finer details are captured with sufficient fidelity. The upper part of the image is quite imprecise, as previously stated, mainly due to the fact that the scan was incomplete.




(a) MIMO MEA result (b) SISO MEA result

Figure 4.6: Imaging results of the second scene using MEA.

After the MEA elaboration, the shape of the scanned object can be clearly observed in both images, except for the upper part due to the problem described previously.

## 4.3 Third scene

For the third acquisition two spheres, with a diameter of 36 mm each, made of solid Teflon material have been put on the test bed. This test assesses the ability of the system to discriminate between non-metallic objects.

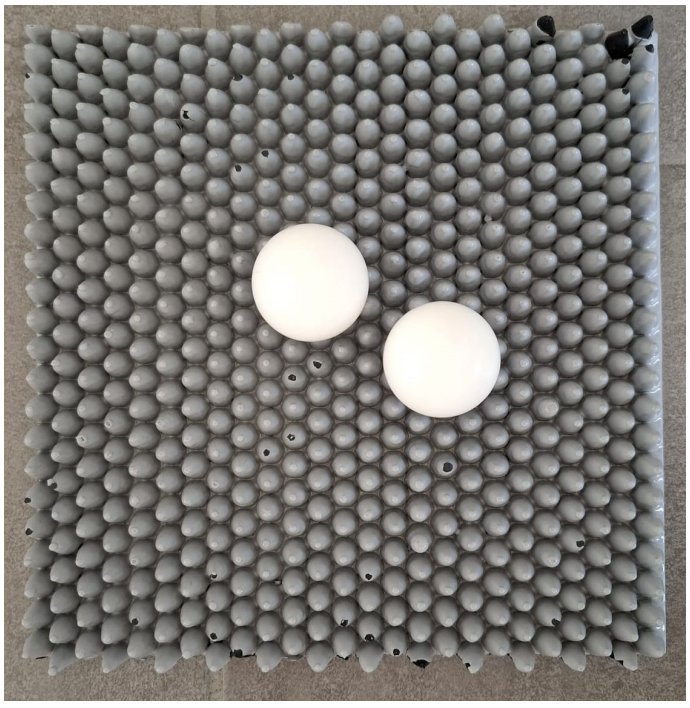
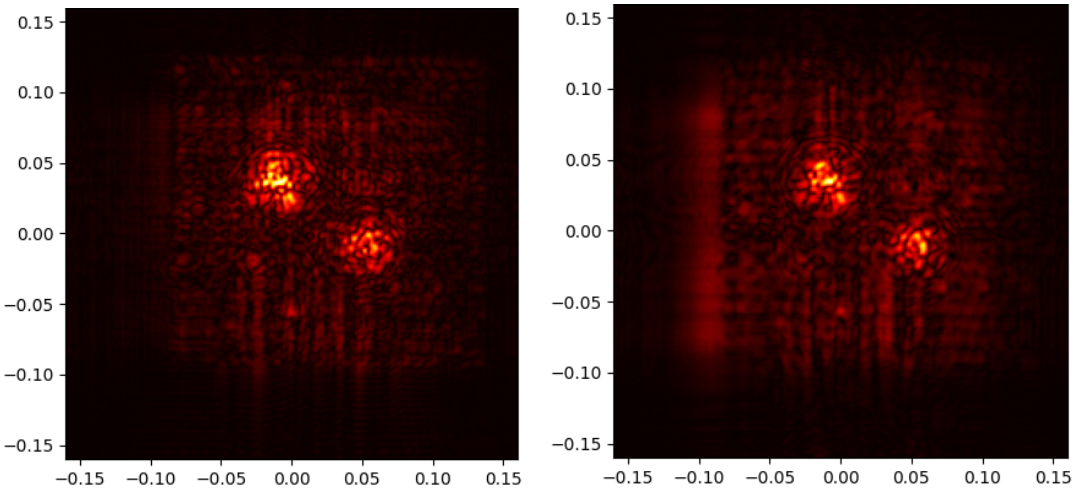


Figure 4.7: Third test acquisition with two Teflon spheres.

In this scenario it was difficult to predict a possible outcome, since the Teflon is a plastic material and therefore does not reflect the waves in a clear way, but it still introduces a discontinuity in the scanned scene, so at least a general idea of the shapes is expected to be seen.

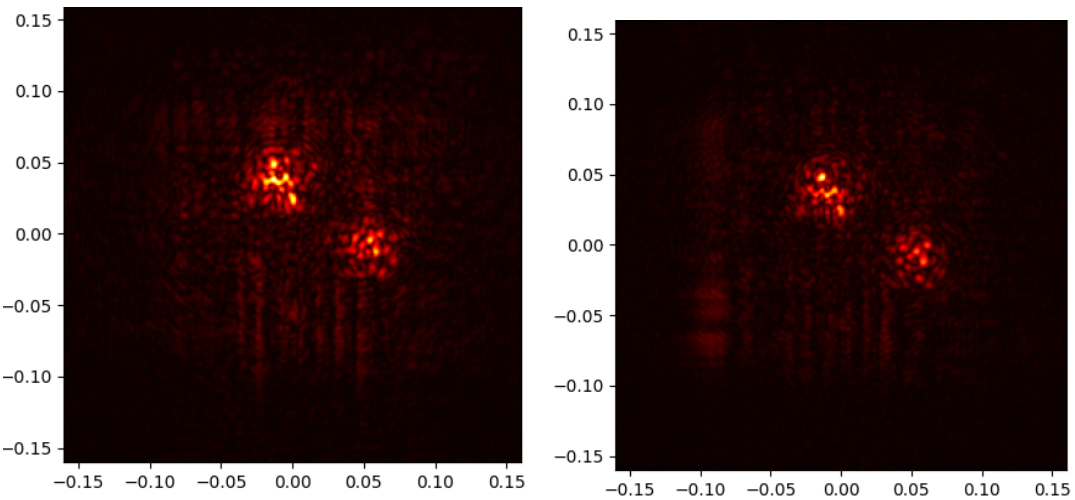



(a) MIMO BPA result (b) SISO BPA result

Figure 4.8: Imaging results of the third scan using only BPA.

In Figure 4.8a and Figure 4.8b it is not as clear as in previous cases what the shape and precise position of the objects are, but it is still possible to have a general idea of their position.

In this case, contrary to the other ones, the MIMO image is much less noisy than the SISO one.




(a) MIMO MEA result (b) SISO MEA result

Figure 4.9: Imaging results of the third scan using MEA algorithm.

After MEA elaboration the position of the spheres is a bit clearer, although the shape is still difficult to define from Figure 4.9a and Figure 4.9b. In this case, a large portion of the background noise is removed

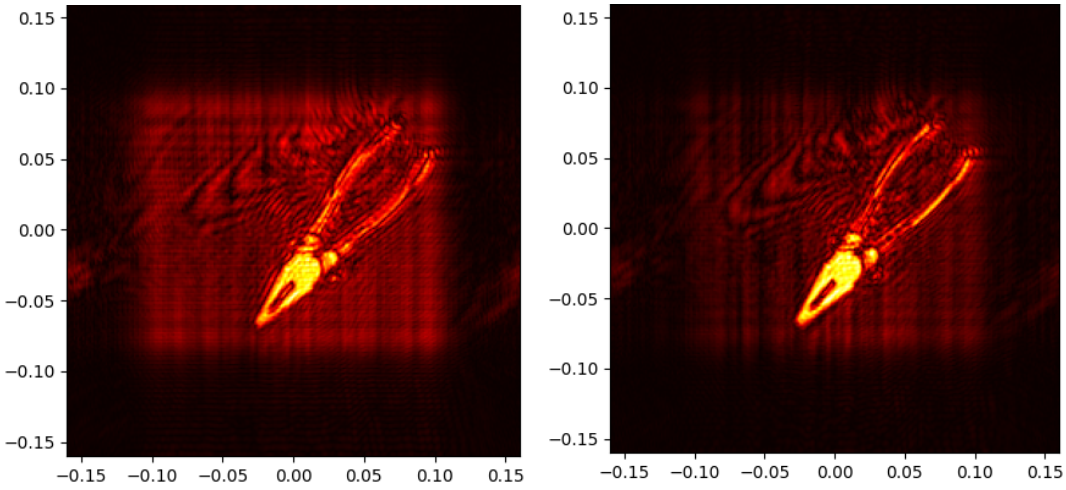
## 4.4 Fourth scene

The last acquisition test has been performed with two metallic objects, as in the case described in Section 4.1, but with the difference that the objects were on different distance levels with respect to the radar. In particular, the pliers was closer to the radar while the screwdriver was around 10 cm more distant from it. In this case the ability of FMCW radars to discriminate objects at different ranges is exploited, trying to recover different images at different distances.




Figure 4.10: Fourth test acquisition with two metallic objects on different levels.

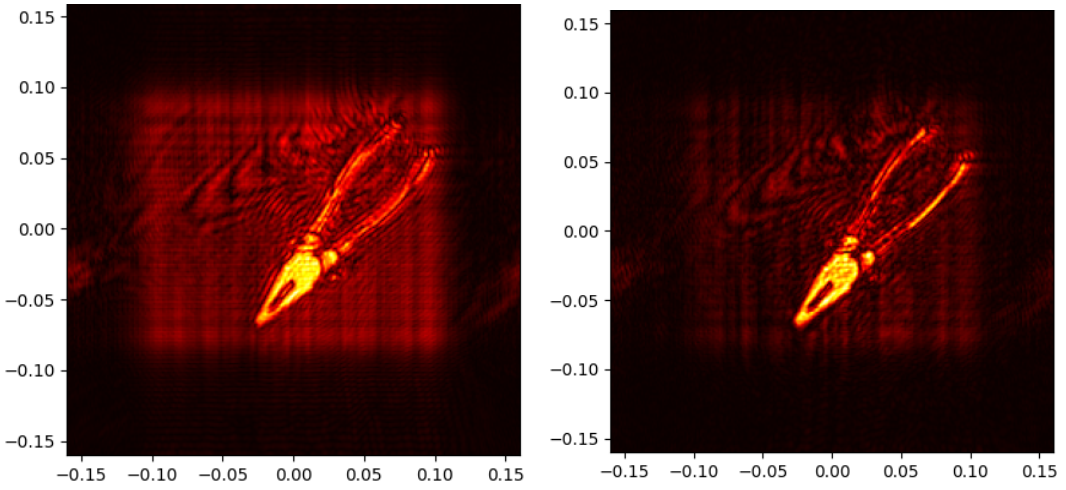
In this scenario, the expected results are quite similar to the first case described, since both objects are made of metallic material.




(a) MIMO pliers BPA result (b) SISO pliers BPA result

Figure 4.11: Imaging results of the fourth scan considering only the pliers using only BPA.

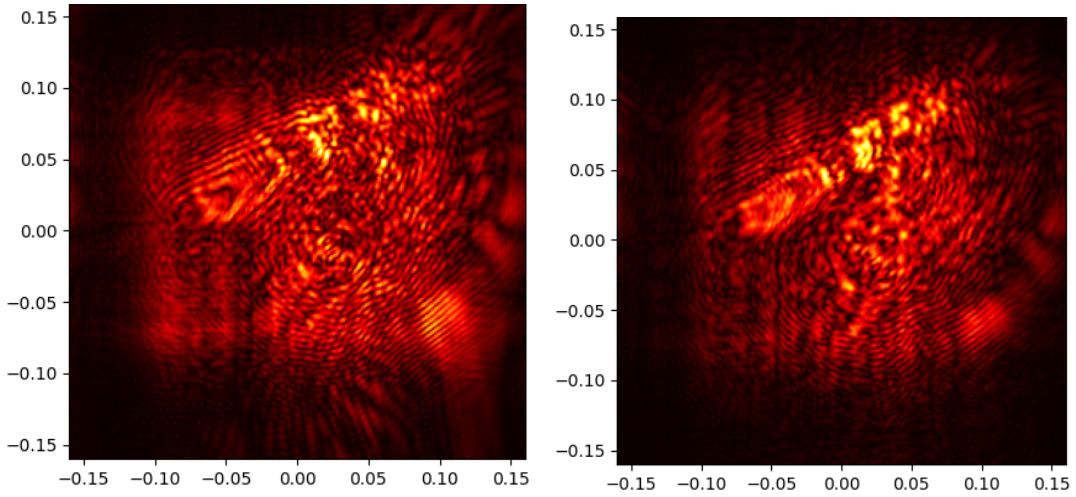
The results of the images in Figures 4.11a- 4.11b were reconstructed at the distance level at which the pliers were expected to be. As expected, the target has a very high contrast with respect to the background, although a bit noisy. Also in this case the SISO image is a bit less noisy than the MIMO one.




(a) MIMO pliers MEA result (b) SISO pliers MEA result

Figure 4.12: Imaging results of the fourth scan considering only the pliers using MEA.

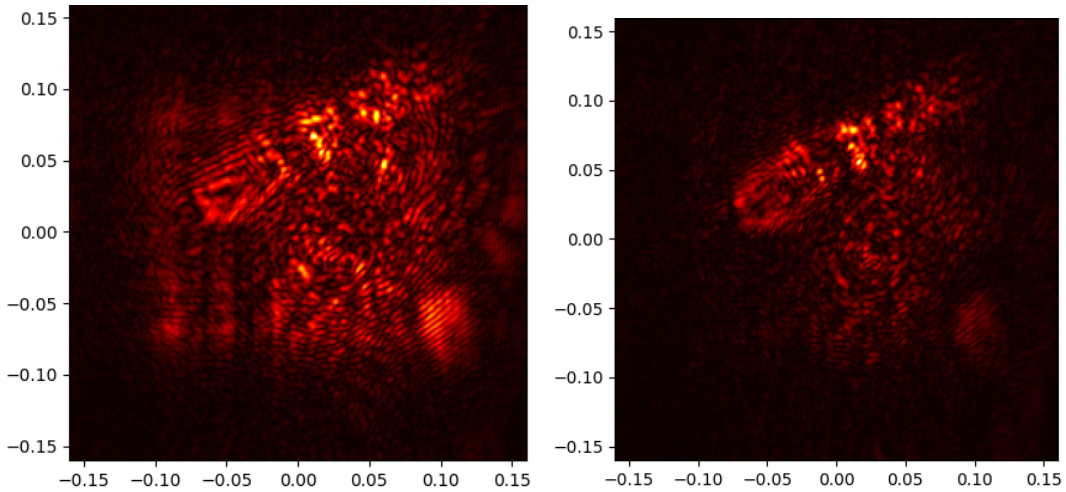
Also in this situation, the MEA is able to remove some noise from the background, creating a higher contrast image. The images remain still quite noisy.




(a) MIMO screwdriver BPA result (b) SISO screwdriver BPA result

Figure 4.13: Imaging results of the fourth scan considering only the screwdriver using only BPA.

This is the first case in which it is actually difficult to distinguish the scanned object, as the resulting image is very noisy and there is no clear shape represented. This is probably due to the fact that a very strong scatterer, such as the pliers, is very close to the radar creating so some echoes and consequently some distortions. Another reason might be the low angle distance between the two objects. Although in the SISO image it is a bit more defined, the shape of the screwdriver is very hard to observe.




(a) MIMO screwdriver MEA result (b) SISO screwdriver MEA result

Figure 4.14: Imaging results of the fourth scan considering only the screwdriver using MEA.

Even after the MEA processing the shape of the screwdriver is very hard to define despite the fact that the background noise is almost totally removed.

Probably, in order to have better images, it would be possible to distance the objects a bit more especially in the angle dimension.

## 4.5 Numerical results

This section complements the visual analysis with a quantitative one. The metric adopted is the Shannon entropy of the normalized image intensity, discussed in Section 2.4, which is low when the energy is concentrated in few pixels and high when it is spread over the image. Since MEA explicitly minimizes this quantity, the entropy reduction in Table 4.1 confirms that the algorithm converges.

The entropy decreases in all ten cases, by 3.0% to 10.5%. The reduction is larger for the MIMO configuration than for the SISO one in every scene, which may indicate that the MIMO data contain more residual phase errors for MEA to correct, probably due to some small miscalibration between the antennas. The highest entropy values belong to the screwdriver images (Fig. 4.14a and 4.14b), consistent with the fact that its shape could not be recognized. Note that entropy and visual noise do not always agree, as also previously mentioned because the pixel color intensity is not in an absolute scale, but in a relative one.

| Scene | Configuration | BPA | MEA | $\Delta H$ | $\Delta H/H_{\mathrm{BPA}}$ (%) |
|---|---|---|---|---|---|
| 1 | MIMO (Fig.4.3a) | 12.09 | 11.02 | −1.07 | −8.9 |
| | SISO (Fig.4.3b) | 11.76 | 10.97 | −0.79 | −6.7 |
| 2 | MIMO (Fig.4.6a) | 13.37 | 12.26 | −1.11 | −8.3 |
| | SISO (Fig.4.6b) | 13.25 | 12.21 | −1.04 | −7.8 |
| 3 | MIMO (Fig.4.9a) | 13.49 | 12.08 | −1.41 | −10.5 |
| | SISO (Fig.4.9b) | 12.99 | 12.21 | −0.78 | −6.0 |
| 4, pliers | MIMO (Fig.4.12a) | 12.76 | 11.97 | −0.79 | −6.2 |
| | SISO (Fig.4.12b) | 13.88 | 13.47 | −0.41 | −3.0 |
| 4, screwdriver | MIMO (Fig.4.14a) | 14.25 | 13.17 | −1.08 | −7.6 |
| | SISO (Fig.4.14b) | 14.49 | 13.94 | −0.55 | −3.8 |

Table 4.1: Image entropy after BPA and after MEA processing.

# Chapter 5

# Conclusions

This Thesis addressed the implementation of a system for near-field SAR image reconstruction. After reviewing the principles of FMCW radar and SAR imaging and discussing why far-field algorithms are not applicable at short range, a complete acquisition and processing chain was developed. The system combines the IWR6843AOP 60 GHz MIMO radar, operated in TDM, with a mechanical structure that scans the target over an area of about $22 \times 19$ cm with a step of $\lambda/4 = 1.25$ mm. The images are reconstructed with a Fourier-domain variant of the well known BPA that reduces the processing time by a very large factor at the cost of a lower accuracy in the range compression. A MEA elaboration, which estimates a scalar phase correction for each frame, is then applied to compensate the residual phase errors.

The experimental campaign, performed inside a working office with several potential noise sources, showed that the system reconstructs metallic objects clearly. In almost all the cases, except for the screwdriver in the fourth presented scene, the metallic objects were clearly visible over the rest of the reconstructed grid; even though the outcome of the third experiment was difficult to predict, the results – especially after the MEA– showed consistency with the real scene. MEA consistently increased the contrast of the images and removed most of the residual background energy, and the image entropy decreased in all ten cases, by 3.0% to 10.5%, with a larger reduction for the MIMO configuration than for the SISO one in every scene. Moreover, the MIMO configuration did not always outperform the SISO one visually, and the fourth receiving antenna had to be excluded because of the distortions it introduced. It should finally be noted that the entropy is the quantity minimized by MEA, so its reduction confirms the behavior of the algorithm rather than providing an independent measure of the image quality, and that the comparison among configurations remains largely qualitative. Overall, the results indicate that BPA combined with entropy-based autofocus is a viable approach for short-range imaging with low-cost millimeter-wave hardware.

## 5.1 Possible applications

The compactness, the low cost, and the fine range resolution of integrated millimeter-wave radars make the presented approach suitable for several short-range imaging applications. In security screening, the ability to reveal both metallic and, to a limited extent, non-metallic objects, as shown by the tools and by the Teflon spheres of

the experiments, is relevant to the inspection of items and people at close distance without the use of ionizing radiation. In non-destructive testing, the clear reconstruction of the complex metallic object suggests the possibility of inspecting the shape and the integrity of metallic parts and structures, or detecting the presence of objects that are not directly visible, in an industrial context where low-cost and contactless sensors are of interest. Compact biomedical imaging is a further field in which a near-field radar with a small footprint could be employed. More generally, the same acquisition and processing chain can be adapted to any scenario in which a small radar can be moved over a limited area in front of a target, for example in robotic platforms or laboratory setups for material and object characterization. The feasibility of each application would require dedicated experiments with realistic targets and requirements.

## 5.2 Future improvements

Several improvements can be considered to extend the present work. On the acquisition side the scanning time is currently a limiting factor: faster mechanics, a scanning strategy with continuous motion or a sparser sampling of the grid could reduce it, provided that the sampling criterion on the step size is taken into account. The Z-axis motor of the structure, which was not used in this work, could be exploited to acquire data at multiple heights, obtaining a true three-dimensional aperture and a better discrimination of objects at different distances, such as the pliers and the screwdriver of the fourth scene. The hardware itself can be better exploited by calibrating the receiving channels and recovering the fourth receiving antenna, and by using all the three transmitting elements to increase the number of virtual elements from the current six to twelve. A more accurate positioning, for instance through feedback on the motion of the stepper motors, would also reduce the phase errors at the source.

On the processing side, the autofocus stage could be improved by allowing more iterations with a strategy that prevents the distortions for high iteration counts, such as adaptive step sizes or regularization, and by reducing its computational cost, for instance through a parallel implementation of the entropy evaluation. A comparison with other autofocus techniques and a more complete study of the range compression, including the use of windowing to limit the sidelobes of strong scatterers, may improve the images of scenes with targets of very different reflectivity. Finally, a larger experimental campaign with more materials, sizes, and distances, complemented by a quantitative evaluation of the resolution and of the geometric accuracy with respect to known ground truth, would allow the performance of the system to be characterized more rigorously.

# Bibliography


[1] Constantine A. Balanis. *Antenna Theory: Analysis and Design*. 4th ed. Hoboken, NJ: John Wiley & Sons, 2016. ISBN: 9781118642061.

[2] Cesar Iovescu and Sandeep Rao. *The Fundamentals of Millimeter Wave Radar Sensors*. Tech. rep. SPYY005A. Texas Instruments, July 2020. URL: `https://www.ti.com/lit/wp/spyy005a/spyy005a.pdf`.

[3] Eugene F. Knott, John F. Shaeffer, and Michael T. Tuley. *Radar Cross Section*. 2nd ed. Raleigh, NC: SciTech Publishing, 2004. ISBN: 9781891121258.

[4] Thomas J. Kragh and Alaa A. Kharbouch. "Monotonic Iterative Algorithm for Minimum-Entropy Autofocus". In: *Proceedings of the Adaptive Sensor Array Processing Workshop*. Lexington, MA, USA, June 2006.

[5] Giacomo Paterniani et al. "Radar-Based Monitoring of Vital Signs: A Tutorial Overview". In: *Proceedings of the IEEE* 111.3 (2023), pp. 277–317.

[6] Merrill I. Skolnik. *Introduction to Radar Systems*. 3rd ed. New York: McGraw-Hill, 2002. ISBN: 0072881380.

[7] Texas Instruments. *IWR6843AOP Single-Chip 60 to 64 GHz mmWave Sensor Antennas-On-Package (AOP)*. Datasheet SWRS237C, `https://www.ti.com/lit/ds/symlink/iwr6843aop.pdf`. June 2025.

[8] Junfeng Wang and Xingzhao Liu. "SAR Minimum-Entropy Autofocus Using an Adaptive-Order Polynomial Model". In: *IEEE Geoscience and Remote Sensing Letters* 3.4 (2006), pp. 512–516.

[9] Li Xi, Guosui Liu, and Jinlin Ni. "Autofocusing of ISAR Images Based on Entropy Minimization". In: *IEEE Transactions on Aerospace and Electronic Systems* 35.4 (Oct. 1999), pp. 1240–1252.

[10] Muhammet Emin Yanik and Murat Torlak. "Near-Field MIMO-SAR Millimeter-Wave Imaging With Sparsely Sampled Aperture Data". In: *IEEE Access* 7 (2019), pp. 31801–31819.

[11] Yanik, Muhammet Emin and Wang, Dan and Torlak, Murat. "Development and Demonstration of MIMO-SAR mmWave Imaging Testbeds". In: *IEEE Access* 8 (2020), 126019–126038.

[12] Tao Zeng, Rong Wang, and Feng Li. "SAR Image Autofocus Utilizing Minimum-Entropy Criterion". In: *IEEE Geoscience and Remote Sensing Letters* 10.6 (Nov. 2013), pp. 1552–1556.

# Appendix

## Appendix A

The FFT is a well known algorithm to compute in an efficient way the frequency spectrum of a signal, and it is based on the DFT formula. The DFT converts a finite sequence of $N$ equally spaced time-domain samples $x[n] = (x[0], x[1], \ldots, x[N-1])$, as the fast-time samples from the ADC of the radar, into its complex frequency-domain representation $X[k] = (X[0], X[1], \ldots, X[N-1])$. The forward DFT is defined as

$$X[k] = \sum_{n=0}^{N-1} x[n] e^{-j\frac{2\pi}{N}kn}, \quad k = 0, 1, \ldots, N-1 \tag{5.1}$$

where $k$ is the number corresponding to the range bin computed.

Direct computation of all $N$ spectral components requires $N$ operations per frequency bin across $N$ bins, leading to a computational complexity of $\mathcal{O}(N^2)$. There are known algorithms that optimized the computation, as the famous *Cooley-Tukey* method that lower the complexity to $\mathcal{O}(N \log_2 N)$.

Although the accuracy achieved by the FFT is high, it is true only for range bins $k$ with integer values. If the real value of $k$, that is proportional to the $f_{beat}$ from the formula $N f_{beat}/f_s$, is a fractional one, as often is the case, and it is necessary to compute the frequency content at the precise distance, as in the case of this Thesis, the DFT must be computed manually. This obviously implies that the correct distance need to be computed, that is very computationally expensive, and also the unoptimized DFT has to be calculated.

## Appendix B

The image reconstruction algorithms presented in Section 2.3 rely on coherently combining the backscattered data acquired at a discrete set of antenna positions along the scanning axes. As with any discrete acquisition of a continuous signal, the spacing between these positions must satisfy a sampling criterion in order to avoid aliasing artifacts in the reconstructed image. This section derives the maximum admissible step size $d_x$ (and $d_y$) for the mechanical scanning structure described in Section 3.2.

Consider a point scatterer located at position $(x, y, z)$ and an antenna moving along the scanning axis, whose transmitting and receiving elements are located, respectively, at $(x_T, y_T, Z_0)$ and $(x_R, y_R, Z_0)$. For the sake of simplicity the phase-center approximation can be applied, so that $R_T \approx R_R \approx R$, where $R$ is the one-way

distance between the antenna and the target. Under this approximation, the round-trip phase term introduced in Equation (2.18) becomes [10]

$$\phi(x) \approx 2kR(x), \tag{5.2}$$

where $k = 2\pi f/c$ is the wavenumber corresponding to the instantaneous frequency $f$.

For a target located at an angle $\theta$ with respect to the broadside direction of the scanning axis, a differential displacement $d_x$ of the antenna produces a corresponding change in the one-way distance of $d_R = \sin\theta\, d_x$. The spatial phase gradient with respect to the antenna position is therefore

$$\frac{d_\phi}{d_x} = 2k\sin\theta. \tag{5.3}$$

This quantity represents the local spatial frequency of the signal as a function of antenna position, and it reaches its maximum value when targets are imaged up to the widest angular extent of interest, $\theta_{max} = 90°$, corresponding to

$$\left(\frac{d_\phi}{d_x}\right)_{max} = 2k_{max} = \frac{4\pi}{\lambda}, \tag{5.4}$$

where $\lambda = c/f$ is the wavelength at the highest operating frequency of the chirp.

According to the Nyquist sampling theorem, a signal with maximum spatial angular frequency $\left(\frac{d_\phi}{d_x}\right)_{max}$ can be sampled without aliasing only if the sampling interval satisfies

$$d_x \leq \frac{\pi}{\left(\frac{d_\phi}{d_x}\right)_{max}}. \tag{5.5}$$

Substituting Equation (5.4) into Equation (5.5) yields the maximum admissible step size for the scanning structure:

$$d_x \leq \frac{\lambda}{4}. \tag{5.6}$$

The same reasoning applies independently to the $y$-axis, so that $d_y \leq \lambda/4$ as well.

If this condition is violated, the synthetic aperture is undersampled with respect to its own spatial frequency content, and the reconstructed image exhibits aliasing artifacts in the form of grating lobes, that is, spurious replicas of the true scatterer appearing at other angular positions within the reconstructed scene. This directly motivates the choice of step size adopted for the mechanical scanning structure described in Section 3.2, and it also explains why even small mechanical errors in the stepper motor motion, comparable in magnitude to $d_x$ itself, can noticeably degrade the focus of the reconstructed image, a problem that the autofocus algorithm presented in Section 2.4 is designed to mitigate.